Journal of Fluids and Structures 17 (2003) 561–577

JOURNAL OF FLUIDS AND STRUCTURES

www.elsevier.nl/locate/jnlabr/yjfls

Numerical study of incompressible flow about fixed cylinder pairs

W. Jester, Y. Kallinderis*

Department of Aerospace Engineering and Engineering Mechanics, The University of Texas at Austin, Austin, TX 78727, USA

Received 1 December 2001; accepted 23 October 2002

Abstract

A comprehensive numerical investigation of incompressible flow about fixed cylinder pairs is performed. Cylinder arrangements include tandem, side-by-side, and staggered and Reynolds numbers of 80 and 1000 are considered. A second order Streamline Upwind Petrov–Galerkin projection scheme is used along with routines for interactive steering and dynamic meshing to solve the 2-D incompressible Navier–Stokes equations efficiently on a large number of different configurations. Qualitative and quantitative comparisons with published experimental data are made which show the ability of the present numerical method to capture complex, unsteady flow features. Experimentally observed flow physics such as hysteresis effects in tandem arrangements and bistable biased gap flow in tandem arrangements have been reproduced by the present numerical method. Furthermore, an extensive series of staggered simulations in experimentally classified interference regimes has been performed.

1. Introduction

Many engineering structures such as offshore risers, pipelines, and transmission lines involve multiple bluff bodies in proximity. Depending on the configuration of these bodies relative to the flow, a wide variety of interference phenomena can be observed. Even the simplest case of two identical circular cylinders presents a rich spectrum of different flow features.

This paper describes a comprehensive numerical investigation of interference effects between rigid circular cylinders in a uniform, 2-D incompressible flow. To enable the most complete and efficient analysis of the problem, routines for interactive simulation and dynamic meshing have been coupled to an accurate and efficient incompressible flow solver. These interactive techniques allow a detailed study of transitions between flow states and hysteresis effects, as well as rapid simulation of a large number of cylinder spacings.

1.1. Previous work

The problem of flow about cylinder pairs has attracted a great deal of research experimentally and, more recently, numerically. Experimental work dates back to early aeronautical experiments by Pannell et al. (1915) on wires and Biermann and Herrnstein (1933) on aircraft struts. Results are presented for *tandem* arrangements in which one cylinder is directly in the wake of the other, *side-by-side* arrangements in which the cylinders are arranged transverse to the incoming flow, and *staggered* arrangements in which the cylinders are arbitrarily configured. Both the

*Corresponding author. Tel.: +1-512-471-4190.
E-mail address: kallind@mail.utexas.edu (Y. Kallinderis).

0889-9746/03/$ - see front matter
PII: S0889-9746(02)00149-4

flow field and force coefficients depend highly on the configuration and spacing of the cylinder pair due to both wake and proximity-induced interference effects. Excellent summaries of results in each of these arrangements can be found in works by Zdravkovich (1984, 1985), Chen (1987), Blevins (1990) and Sumner et al. (2000).

Experimental studies of cylinder pairs in a tandem orientation presented by Thomas and Kraus (1964), Nagai and Kurata (1971), Ishigai et al. (1972), Kostic and Oka (1972), Tanida et al. (1973) and King and Johns (1976) demonstrate the presence of two major flow regimes with a complex transition region between them. For closely spaced cylinders, the flow separates behind the first cylinder and reattaches to the second one, while for larger separations vortex shedding occurs behind both cylinders. For intermediate spacings, flow physics such as hysteresis effects (Zdravkovich, 1984) and bi-stable states (Kiya et al., 1992) have been observed experimentally. Similarly, studies of side-by-side cylinder pairs performed by Bearman and Wadcock (1973), Kiya et al. (1980), Zdravkovich (1982) and Williamson (1985) show two major flow regimes. Closely spaced cylinder pairs exhibit a single coupled vortex street while more distant cylinders shed distinct but synchronized vortices in their wake. Again, intermediate spacings lead to complex flow physics such as the bi-stable biased gap flow observed by Kim and Durbin (1988). Staggered arrangements of cylinder pairs show a combination of both the wake-induced interference found in the tandem configuration and proximity-induced interference in the side-by-side configuration. Classification of these effects in a variety of spacings has been performed by Zdravkovich (1977, 1984).

Numerical work on this problem is considerably more sparse. Chang and Song (1990) used a vorticity-stream-function method to compute the flow about a pair of cylinders in two arrangements at $\mathrm{Re} = 100$. Flow visualization and force coefficients were shown to compare well with experimental publications. More recently, Mittal et al. (1997) used a stabilized finite element method to simulate three configurations at $\mathrm{Re} = 100$ and 1000. Again, good comparison with experimental results was made; furthermore the results showed that $\mathrm{Re} = 1000$ flow was sufficient to reproduce flow features observed in experimental results gathered at a much higher Reynolds number. Finally, Schulz and Kallinderis (1998a) used a finite volume method to compute the flow and structural response for a single arrangement at $\mathrm{Re} = 110$.

1.2. Organization of paper

A more detailed description of the problem and the governing equations will first be given in Section 2. Next, in Section 3 we will briefly describe the numerical method used to solve the incompressible Navier–Stokes equations in addition to the interactive simulation and mesh update routines used for the interactive runs. In Section 4 we present extensive numerical results for a variety of different configurations including both quantitative and qualitative comparisons with experimental data. Finally, in Section 5 we draw some conclusions and propose future work.

2. Problem definition

The problem being considered is flow about a pair of identical circular cylinders. Fig. 1 shows the two cylinders of diameter D with longitudinal separation L and transverse separation T relative to the incoming flow U_∞.

In the description of results found in this paper, the nondimensional values L/D and T/D will be used to identify the configuration. Results will be presented for *tandem* orientations with $T/D = 0$, *side-by-side* orientations with $L/D = 0$, and *staggered* orientations with $L/D \neq 0$, $T/D \neq 0$.

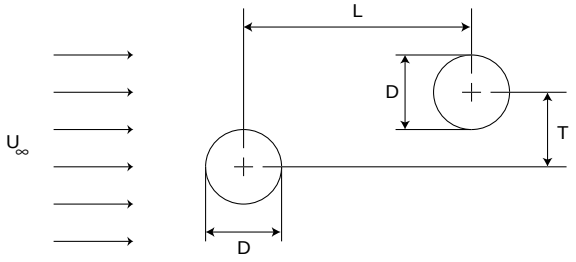

Fig. 1. Configuration of cylinder pair.

The flow is assumed to be 2-D and governed by the unsteady incompressible Navier–Stokes equations in Arbitrary Lagrangian–Eulerian form (Hughes et al., 1981):

$$\frac{\partial \mathbf{u}}{\partial t} + (\mathbf{u} - \hat{\mathbf{u}}) \cdot \nabla \mathbf{u} = -\nabla P + \frac{1}{\mathrm{Re}} \nabla^2 \mathbf{u}, \tag{1}$$

$$\nabla \cdot \mathbf{u} = 0, \tag{2}$$

where $\mathbf{u}$ is the flow velocity vector, $\hat{\mathbf{u}}$ is the *mesh velocity*, P is the pressure, and Re is the Reynolds number, defined by

$$\mathrm{Re} = \frac{U_\infty L}{v}. \tag{3}$$

Dirichlet boundary conditions are enforced on the inlet and farfield boundaries while Neumann conditions are imposed on the outlet.

3. Numerical method

3.1. Finite element formulation

The mixed finite element solution of Eqs. (1) and (2) is sought. Let $\mathbf{V}^h \equiv \mathbf{V}^h(\Omega) \subset \mathbf{H}^1(\Omega)$ and $S^h \equiv S^h(\Omega) \subset L^2(\Omega)$ be finite element spaces approximating the velocity and pressure, respectively, on domain Ω where Dirichlet boundary conditions are accounted for in the velocity space. The semi-discrete finite element form of the Navier–Stokes equation is: find $\mathbf{u}^h \in \mathbf{V}^h$ and $p^h \in S^h$ such that

$$\int_\Omega \mathbf{w}^h \cdot \left(\frac{\partial \mathbf{u}^h}{\partial t} + (\mathbf{u}^h - \hat{\mathbf{u}}^h) \cdot \nabla \mathbf{u}^h \right) \mathrm{d}\Omega + \frac{1}{\mathrm{Re}} \int_\Omega \nabla \mathbf{w}^h : \nabla \mathbf{u}^h \, \mathrm{d}\Omega + \int_\Omega \nabla \cdot \mathbf{w}^h p^h \, \mathrm{d}\Omega = 0 \forall \ \mathbf{w}^h \in \mathbf{V}^h, \tag{4}$$

$$\int_\Omega q \nabla \cdot \mathbf{u}^h \, \mathrm{d}\Omega = 0 \quad \forall \ q \in S^h. \tag{5}$$

Using the standard notation for mass, advection, diffusion, and gradient matrices leads to the following condensed form:

$$\mathbf{M}\dot{\mathbf{u}} + (\mathbf{K} + \mathbf{N}(\mathbf{u} - \hat{\mathbf{u}}))\mathbf{u} + \mathbf{C}P = 0, \tag{6}$$

$$\mathbf{C}^{\mathrm{T}}\mathbf{u} = 0. \tag{7}$$

3.2. Projection method

The semi-consistent mass projection scheme introduced by Gresho (1990) and Gresho and Chan (1990) is the basis for the timestepping scheme used in the present analysis. In contrast to typical semi-implicit projection schemes, the advective term is linearized and treated implicitly while BDF2 timestepping (Guermond and Quartapelle, 1998) is used in place of Crank–Nicolson. The timestepping scheme used is as follows.

Given data at timestep n and $n-1$ ($\mathbf{u}^{n-1}$, $\mathbf{u}^n$ and P^n), solve:

$$\frac{3\mathbf{M}\tilde{\mathbf{u}} - 4\mathbf{M}\mathbf{u}^n + \mathbf{M}\mathbf{u}^{n-1}}{2\Delta t} + \mathbf{K}\tilde{\mathbf{u}} + \mathbf{N}(\mathbf{u}^* - \hat{\mathbf{u}})\tilde{\mathbf{u}} = \ -\mathbf{M}\mathbf{M}_L^{-1}\mathbf{C}P^n \tag{8}$$

for the intermediate velocity $\tilde{\mathbf{u}}$ where $\mathbf{u}^*$ is the extrapolated velocity,

$$\mathbf{u}^* = 2\mathbf{u}^n - \mathbf{u}^{n+1}. \tag{9}$$

Then, compute the final discretely divergence-free velocity $\mathbf{u}^{n+1}$ and the updated pressure P^{n+1} from the projection step:

$$\mathbf{C}^{\mathrm{T}}\mathbf{M}_L^{-1}\mathbf{C}(P^{n+1} - P^n) = \mathbf{C}^{\mathrm{T}}\tilde{\mathbf{u}}, \tag{10}$$

$$\mathbf{u}^{n+1} = \tilde{\mathbf{u}} - \mathbf{M}_L^{-1}\mathbf{C}(P^{n+1} - P^n). \tag{11}$$

Eq. (8) represents nonsymmetric sparse system which is formed at each timestep and solved for each velocity dimension. This system is solved using a diagonally scaled conjugate gradient squared algorithm (Golub and van Loan, 1996). Eq. (10) is solved using an iterative conjugate gradient method proposed by Cahouet and Chabard (1988) for the Stokes problem. The advantage of this method is that it does not require the explicit formation of the pressure poisson Matrix (PPE) on the left-hand side matrix of Eq. (10). Since this matrix must generally be formed globally rather than element-wise, the cost of reassembling it every timestep when using a dynamic mesh can be great (Nomura and Hughes, 1992). Thus, although the algorithm of Cahouet and Chabard involves more effort per timestep to solve, it is far more efficient since the PPE matrix need not ever be explicitly formed.

3.3. SUPG stabilization

The SUPG method of Brooks and Hughes (1982) has been used to allow high Reynolds number simulation on reasonably coarse meshes. This method adds element level residuals to the left-hand side of Eq. (8) of the form

$$\sum_e \int_{\Omega^e} \tau_e^{SUPG} \mathbf{u}^h \cdot \nabla \mathbf{w}^h \left(\frac{\partial \mathbf{u}^h}{\partial t} + \mathbf{u}^h \cdot \nabla \mathbf{u}^h - \frac{1}{\mathrm{Re}} \nabla^2 \mathbf{u}^h - \nabla P^h \right) \mathrm{d}\Omega, \tag{12}$$

where the *doubly asymptotic approximation* is used for the SUPG coefficient

$$\tau_e^{SUPG} = \|\mathbf{u}_e^h\| \frac{h_e}{2} \zeta, \tag{13}$$

$$\zeta = \begin{cases} \dfrac{\mathrm{Re}_h}{3}, & \mathrm{Re}_h \leqslant 3, \\ 1, & \mathrm{Re}_h > 3 \end{cases} \tag{14}$$

and $\|\mathbf{u}_e^h\|$ is the magnitude of the velocity at the centroid of element e, h_e is the average edge length of the element, and Re_h is the cell Reynolds number. This value of the intrinsic time, τ_e^{SUPG} approximates the optimal value for elements with linear velocity approximations (Brooks and Hughes, 1982).

3.4. Hybrid meshes

Hybrid quadrilateral/triangular meshes are used in the present computations. These meshes, an example of which is shown in Fig. 2, consist of a number of layers of stretched quadrilateral elements in boundary layer regions with triangular elements used to fill the rest of the domain. The initial spacing of the quadrilateral layers is set to accurately resolve the flow at the desired Reynolds number. The size of the triangular elements is limited by the definition of source regions which maintain a fine triangulation in areas of interest such as the gap between the cylinders. Meshes of this type have been successfully used in incompressible simulations in both 2-D (Kallinderis and Nakajima, 1994) and 3-D (Chen and Kallinderis, 1998).

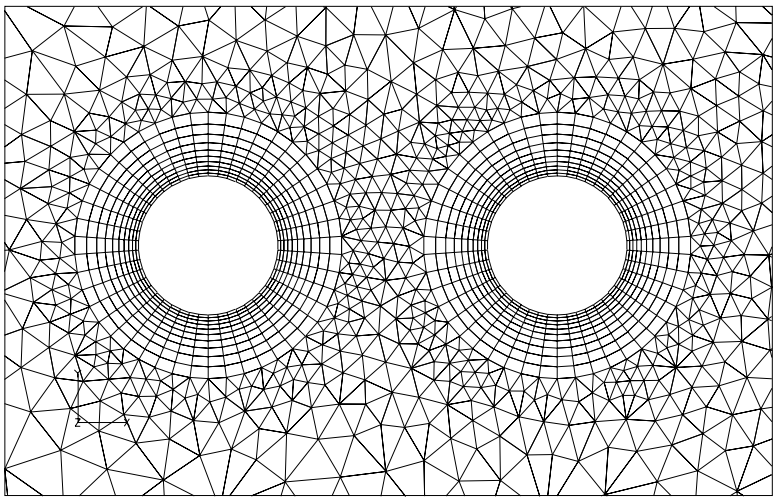

Fig. 2. Closeup of hybrid mesh for a cylinder pair.

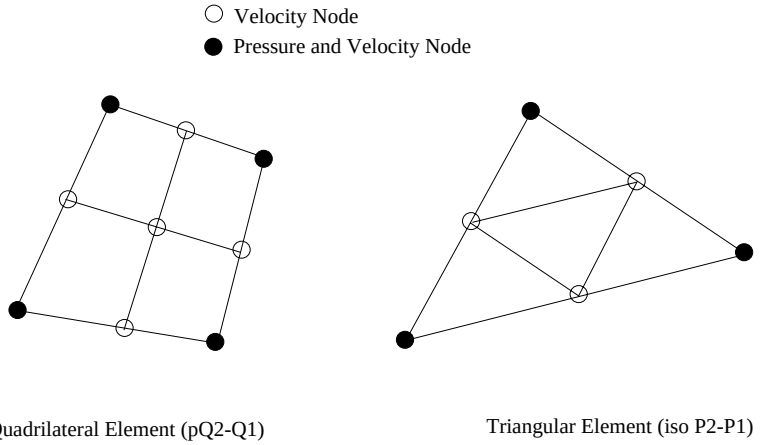

Fig. 3. Quadrilateral and triangular mixed elements.

3.5. Mixed element choices

In the present simulations, the pressure field is approximated as a continuous piecewise (bi)linear function over each (quadrilateral) triangular element. Each pressure element is subdivided into four subelements of the same type, over which a continuous piecewise linear velocity field is interpolated. These mixed elements, shown on Fig. 3, were introduced by Bercovier and Pironneau (1979), analyzed by Verfurth (1984) and Gunzburger (1989), and recently implemented by Norburn and Silvester (1998) and Edis and Aslan (1998) among others. The quadrilateral and triangular elements shown on Fig. 3 are typically referred to as pQ_2Q_1 and isoP_2P_1 elements.

These elements have the same number and location of degrees of freedom as the (bi)quadratic velocity Taylor–Hood elements Q_2Q_1 and P_2P_1. Theoretically, the Taylor–Hood elements give a more accurate velocity solution with the same number of degrees of freedom; however, preliminary work in this analysis showed no difference between the Taylor–Hood elements and their linear counterparts in the class of problems being considered. The linear velocity elements do provide a considerable simplification in implementation of the SUPG method as the second order derivatives $\nabla^2\mathbf{u}$ can be eliminated from Eq. (12). Furthermore, selection of optimal intrinsic times for quadratic elements such as that given for linear elements in Eq. (14) is nontrivial (Codina et al. 1992).

3.6. Interactive steering and mesh motion

To efficiently simulate a large number of different configurations, the ability to interactively manipulate the cylinder spacings during the runs has been provided. This interactive steering has been used extensively in the present research, specifically to study transition regions between states, hysteresis effects, and multiple staggered configurations. Convenient user control over algorithmic parameters such as timestep, physical parameters such as Reynolds number, and geometric parameters such as cylinder spacing has been provided.

Small scale motions of the geometry are handled through a simple smoothing method (Hassan et al., 1998). Other possible methods include *spring analogy* methods (Batina, 1991; Farhat et al., 1998) and *distance function* methods (Schulz and Kallinderis, 1998b). In the present method, the quadrilateral layers surrounding the cylinders translate rigidly with the body while the external boundaries are held fixed. The displacement of the interior nodes is then computed using an iterative, edge based smoothing.

For large scale changes in the geometry, simple mesh deformation is insufficient as elements will rapidly become distorted and the quality of the mesh and solution will suffer. Thus, to accommodate the large scale deformations desired in the present analysis, the mesh topology must change in addition to the geometry. To accomplish this, a series of local adaptations in the mesh is performed at fixed intervals in the simulation. Adaptation is performed to preserve both the quality and area of the elements so highly refined areas such as the gap between the cylinder pair remain refined as the cylinder spacing is changed. The specific forms of adaptation used are edge swapping, edge splitting, element coarsening, and element curing (Trépanier et al., 1993). These adaptations are all performed locally on edges or elements, so no significant remeshing or interpolation is required.

Extensive testing of the adaptation routines and the coupling with the flow solver has been performed. These results indicate that the quality of the mesh is adequately preserved even after a large number of adaptations. Furthermore, although minor discontinuities in derived data (such as lift and drag) are experienced around adaptations, the long term accuracy of the solution is not degraded.

The coupling of simulation and visualization in the present work also allows accurate computation of unsteady particle tracks (streaklines). To produce the flow visualization presented later, massless particles are introduced into the domain at areas of interest and allowed to advect with the flow. In particular, particles are seeded on the cylinders where the flow separates which allows separation and reattachment phenomena to be clearly visible.

4. Results

This section presents the results of numerical simulations for tandem, side-by-side, and staggered configurations of a cylinder pair. In each case, a description of the experimentally observed flow features at various spacings will be given, followed by the present numerical results. Following each case, a summary of the gathered data will be presented in tabular form.

Unless otherwise noted, all cases presented use a Reynolds number of 1000. Although this is far below the typical Reynolds number used in experimental analysis ($\mathrm{Re} = 10^4$–10^5), the majority of relevant flow physics is also found in the more computationally tractable case of $\mathrm{Re} = 1000$. It must be noted that approximating flow at this Reynolds number with the 2-D, laminar, Navier–Stokes equation is unrealistic as both 3-D effects and turbulence are present and significant. As pointed out by Mittal et al. (1997), however, who also performed numerical simulation at $\mathrm{Re} = 1000$, simulations at these lower Reynolds numbers can give excellent insight into the underlying physical phenomena present in real applications. In the case of the present work, experimentally observed interference regimes and flow physics can be demonstrated, although the exact values of transition points and force coefficients cannot be reproduced.

The thickness of the initial quadrilateral layer around both bodies is set to 0.01 for the velocity sub-mesh (normalized by the cylinder diameter). Grid convergence studies at $\mathrm{Re} = 1000$ show that this is sufficiently thin to capture the boundary layer. The triangles in the region between the cylinders and in the near wake of the downstream cylinder are constrained to edge lengths below 0.1. These parameters lead to a grid having between 6000 and 9000 velocity elements depending on the cylinder spacing.

The inflow and outflow boundaries are situated to allow at least 5 diameters between the inflow boundary and the most upstream cylinder and 15 diameters between the outflow boundary and the most downstream cylinder. The farfield boundaries above and below the cylinders are situated to allow at least 8 diameters distance to the closest cylinder.

The timestep was chosen at $\Delta t = 0.05$ which corresponds to a CFL number of 5 based on the minimum velocity element size. The second order implicit projection scheme described in Section 3 produces stable pressure and velocity results even using this large timestep. Convergence studies have determined that this timestep is sufficiently small for the problem and grids being considered. Taking a timestep this large allows a simulation to be performed through over 1000 vortex shedding cycles in a few days so the long-term stability of transient flow regimes can be efficiently studied.

4.1. Isolated cylinder

To validate the numerical method with the stated Reynolds number and mesh parameters, a simulation of an isolated cylinder at $\mathrm{Re} = 1000$ was performed.

For an isolated cylinder at $\mathrm{Re} = 1000$, the mean drag coefficient was found to be $\bar{C}_D = 1.51$, the magnitude of the oscillation in lift was $\tilde{C}_L = 1.40$, and the Strouhal number was $St = 0.25$. Although both the drag and Strouhal number exceed those typically reported in experiments at this Reynolds number (Zdravkovich, 1997), they are consistent with other 2-D numerical simulations (Mittal et al., 1997; Behr et al., 1993, Lei et al., 2000). 3-D simulations of finite length cylinders by Schulz and Kallinderis (2000) at $\mathrm{Re} = 10^4$ demonstrated that 3-D phenomena such as *oblique shedding* can impact average force coefficients, although the flow features of a 2-D simulation and a slice of a 3-D simulation are nearly identical. Thus, the 2-D simulations in the present work are sufficient to study the flow physics underlying the given problem.

4.2. Low Reynolds number tandem configuration

The first series of simulations of tandem cylinder pairs was performed at a low Reynolds number of $\mathrm{Re} = 80$. This Reynolds number was chosen to match the parameters of Tanida et al. (1973) who studied the lift and drag coefficients

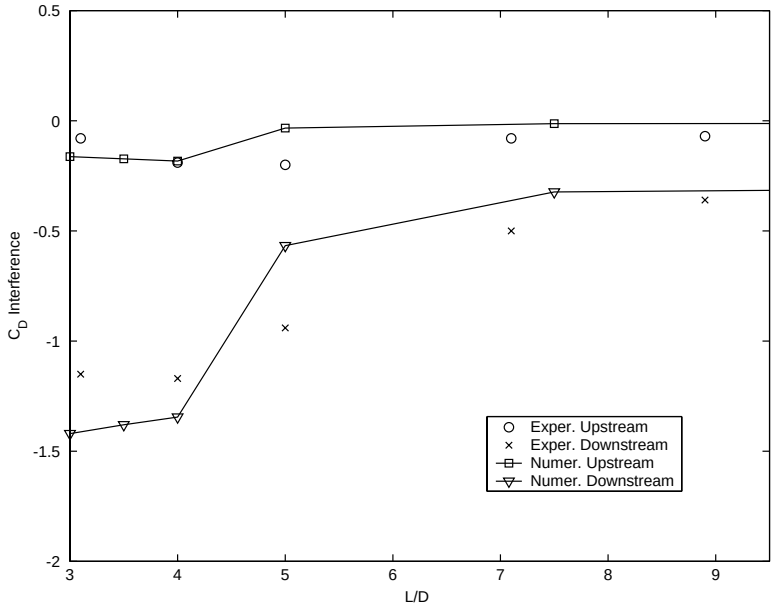

Fig. 4. Interference drag for tandem cylinder pairs at $Re = 80$. Comparison with experimental results of Tanida et al., 1973.

on a pair of tandem cylinders in flowing oil at a variety of spacings. The interference drag (the measured drag minus the drag of an isolated cylinder at the same Reynolds number) for the upstream and downstream cylinders for L/D between 3 and 10 is shown in Fig. 4 for both the experimental and present numerical results. The upstream cylinder (top line) quickly approaches zero interference drag as the spacing is increased, indicating a rapid decline of interference effects.

The downstream cylinder (bottom line) experiences an extreme reduction in drag when in close proximity to the upstream cylinder. As the cylinders are separated, the downstream cylinder approaches an interference drag of roughly -0.3 in both the experimental and numerical results. This reduction in drag, due to the retarded flow about the downstream cylinder, is shown experimentally to persist even to a separation of $L/D = 20$. (Tanida et al., 1973)

4.3. High Reynolds number tandem configuration

At higher Reynolds numbers, three main flow regimes are observed for tandem configurations, depending on the longitudinal separation L/D. According to the classification described by Zdravkovich (1982) and Chen (1987), these flow regimes are as follows.

(i) *Single body* ($L/D \leqslant 1.1$). For tandem cylinders in extremely close proximity, the shear layers separating from the upstream cylinder completely engulf the downstream cylinder. Thus, the two cylinders essential behave as a single body.

(ii) *Reattachment* ($1.1 < L/D < 3.0$–3.8). For larger separations, the shear layers separating from the upstream cylinder reattach to the downstream cylinder. Vortex shedding is observed behind the downstream cylinder but not from the upstream cylinder. A steady recirculation region consisting of a pair of counter-rotating vortices exists in the gap.

(iii) *Two vortex streets* ($L/D > 3.0$–3.8). For large spacings, vortex shedding is observed behind both cylinders. Interference effects on the upstream cylinder are negligible, although wake-interference continues to affect the downstream cylinder even for L/D beyond 50 (Zdravkovich, 1984).

The experimental classifications also include a bistable transition region between the *reattachment* and *two vortex streets* flow regimes. In this transition region, both flow regimes are observed in experiments, with *flopping* between them observed at irregular intervals (Kiya et al., 1992).

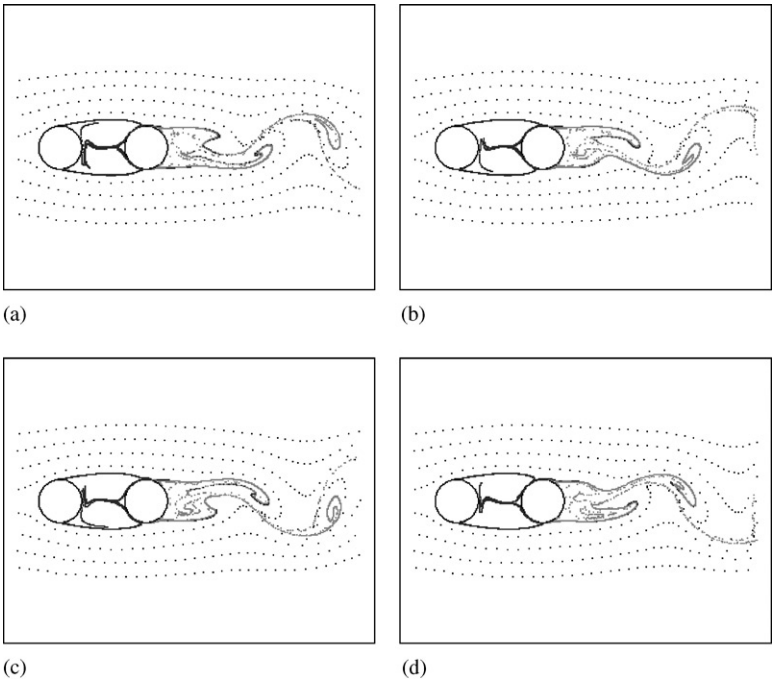

Fig. 5. Particle traces for *reattachment* regime, Re = 1000, $L/D = 2$.

There is a great deal of discrepancy in the literature on the exact longitudinal spacing L/D which marks the boundary between the *reattachment* and *two vortex streets* regimes. Quoted values range from 3.0 (Kiya et al., 1980; King and Johns, 1976) to 3.8 (Zdravkovich, 1977), all at roughly the same Reynolds number ($\mathrm{Re} \approx 10^4$). This scatter of data is likely due to the extreme sensitivity of the flow to Reynolds number, turbulence, and experimental setup and initial conditions.

In the present study, the *reattachment* and *two vortex streets* flow regimes have been simulated in addition to the transition region between them. Due to the strong influence of parameters such as free-stream turbulence and Reynolds number and the lack of experimental data at this Reynolds number, no direct quantitative comparisons can be made. Qualitative comparisons with experimental observations, however, are all good.

4.3.1. Reattachment regime

Four snapshots of particle traces for a tandem arrangement in the *Reattachment* regime ($L/D = 2$) are shown in Fig. 5. As observed in experiments, vortices are alternatively formed and shed behind the downstream cylinder while a stagnant recirculation region exists in the gap. The shear layers from the upstream cylinder reattach to the downstream cylinder with the exact reattachment points oscillating in tune with the vortex formation.

In agreement with experiment, the low-pressure stagnant flow between the cylinders causes a negative drag of $\bar{C}_D = -0.39$ on the downstream cylinder, i.e., the force in-line with the flow acts to pull the downstream cylinder towards the upstream one. The fluctuating lift on the downstream cylinder is $\tilde{C}_L = 0.12$. As the flow visualization in Fig. 5 shows, vortex formation occurs several diameters away from the downstream cylinder which results in less severe oscillations in lift. For the upstream cylinder, the lack of vortex shedding reduces the mean drag to $\bar{C}_D = 0.92$ and minimizes the fluctuating lift to $\tilde{C}_L = 0.04$. The Strouhal number for the downstream cylinder is $St = 0.17$ which indicates vortex shedding is occurring significantly slower than for an isolated cylinder.

4.3.2. Two vortex streets regime

Four snapshots of particle traces in the *two vortex streets* regime ($L/D = 2.5$) are shown in Fig. 6. In this configuration, it is clear that vortices are being formed and shed from both cylinders. The vortices shed from the upstream cylinder rapidly deform as they approach the downstream cylinder while an irregular vortex street is formed in the wake of the downstream cylinder.

The lift and drag coefficients on the cylinders again shows excellent agreement with experimental observations. The downstream cylinder experiences a reduced drag of $\bar{C}_D = 0.17$ due to the retarded wake flow, while the magnitude of lift

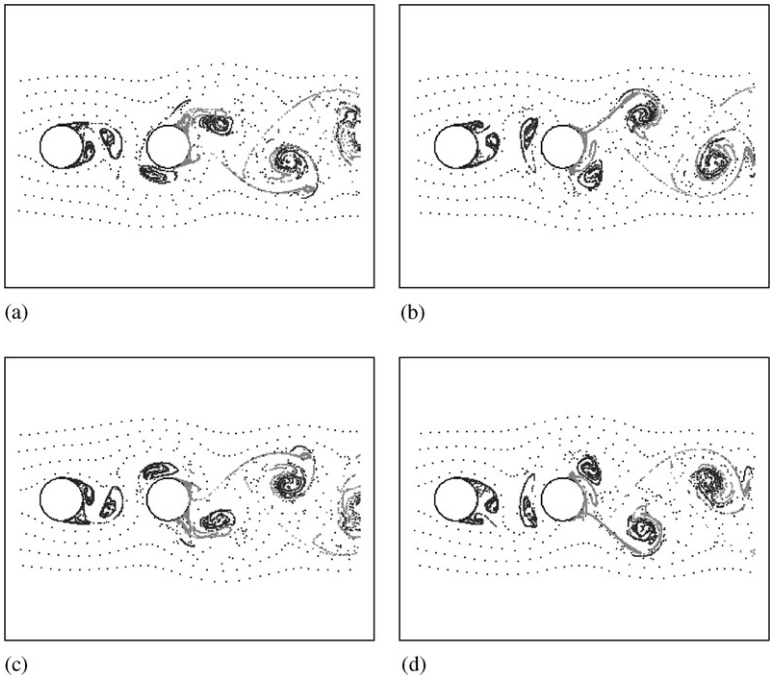

Fig. 6. Particle traces for *two vortex streets* regime, Re = 1000, $L/D = 2.5$.

on that cylinder of $\tilde{C}_L = 2.24$ exceeds that of an isolated cylinder due to the synchronization of vortex shedding behind both cylinders. The upstream cylinder experiences lift and drag coefficients much closer to that of an isolated cylinder ($\bar{C}_D = 1.43$, $\tilde{C}_L = 1.35$), while the Strouhal number for both cylinders is $St = 0.22$, slightly below the isolated cylinder value.

4.3.3. Transition region

For certain tandem separations between $L/D = 2$ and $L/D = 2.5$, the *bistable* nature of the flow has been observed numerically. For $L/D \approx 2.15$, it is possible to drive the flow into either the *reattachment* or *two vortex streets* regimes by selecting the initial conditions.

To achieve the *reattachment* regime, a steady solution at Re = 100 is first obtained. This lower Reynolds number result establishes the steady recirculation region between the cylinders. The Reynolds number is then slowly increased to Re = 1000. The resulting flow pattern, shown in Fig. 7(a), clearly indicates the *reattachment* regime. This state was observed to be stable in the sense of persisting for over 1000 periods of vortex shedding.

To achieve the *two vortex streets* regime, the flow is impulsively started at Re = 1000. In this case, the small asymmetry in the mesh is sufficient to cause vortex shedding from the upstream cylinder to begin before the steady recirculation region can be fully established. The final flow pattern, shown in Fig. 7(b), indicates the *two vortex streets* regime. As before, this state persisted for over 1000 periods of vortex shedding.

Kiya et al. (1992) studied this bistable transition region at a Reynolds number of $\mathrm{Re} \approx 3 \times 10^4$ and showed that *flops* between the regimes occurred on the order of every 10^3–10^4 shedding periods. The average time interval for which each regime is observed was shown to increase as the Reynolds number or freestream turbulence was decreased. Thus, for the laminar flow at Re = 1000 considered here, the two regimes will be stable for extremely long periods of time. Thus, no *flopping* between the states should be expected and none is observed.

4.3.4. Hysteresis

Another experimentally observable feature in the tandem orientation is the presence of a hysteretic effect. This is well summarized by the following quote from Zdravkovich (1984):

> One of the two flow regimes persisted longer when the velocity was increased or, at the same velocity when the cylinder was displaced in one direction, and the other regime lasted longer when the opposite conditions were

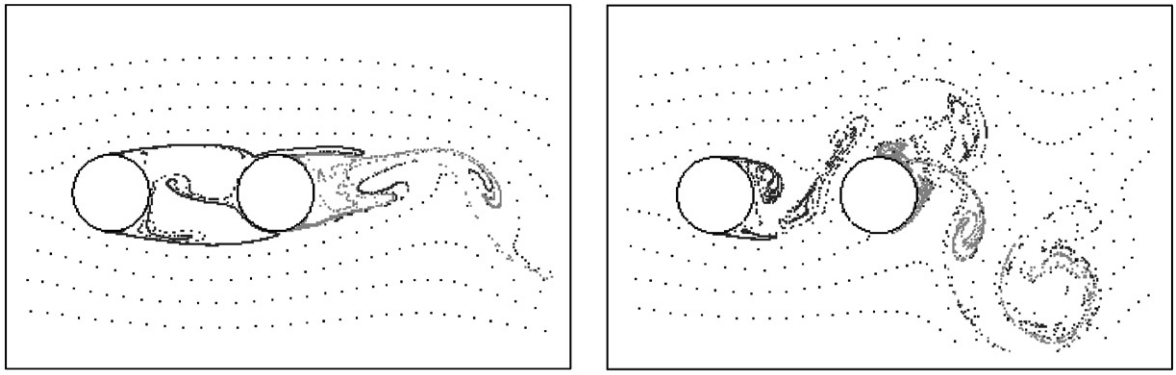

(a) Reattachment Regime (b) Two Vortex Streets Regime

Fig. 7. Particle traces in bistable region, Re = 1000, $L/D = 2.15$.

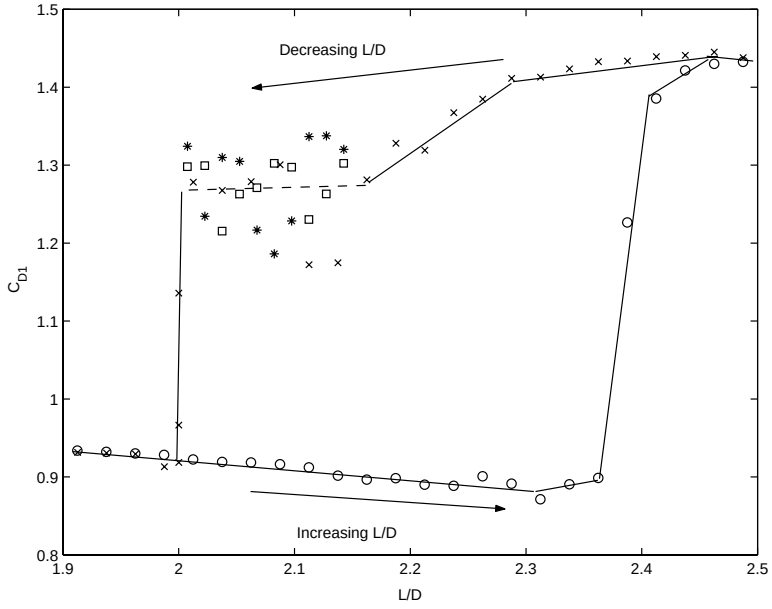

Fig. 8. Hysteresis of upstream drag coefficient, Re = 1000.

imposed. The hysteresis produced an apparent overlap of the two flow regimes although only one flow regime existed at a time.

Using the interactive steering and dynamic mesh deformation/adaptation described in Section 3.6, it is possible to numerically observe this hysteresis phenomenon. Fig. 8 and 9 show the drag coefficient on the upstream and downstream cylinder as a function of L/D for either an increasing spacing (shown as circles) or decreasing spacing (shown as exes).

The lower branch of the hysteresis is achieved by starting in the *reattachment* regime at $L/D = 1.9$ and slowly increasing the spacing to $L/D = 2.5$ by moving the downstream cylinder at a velocity of 0.1% of the freestream velocity. As Figs. 8 and 9 show, the *reattachment* regime is observed up to a spacing of $L/D \approx 2.38$ at which point a rapid transition to the *two vortex streets* regime occurs. This transition is indicated by a sharp increase in the drag coefficients for both cylinders, consistent with experimental observations. The exact spacing of this transition differs from the

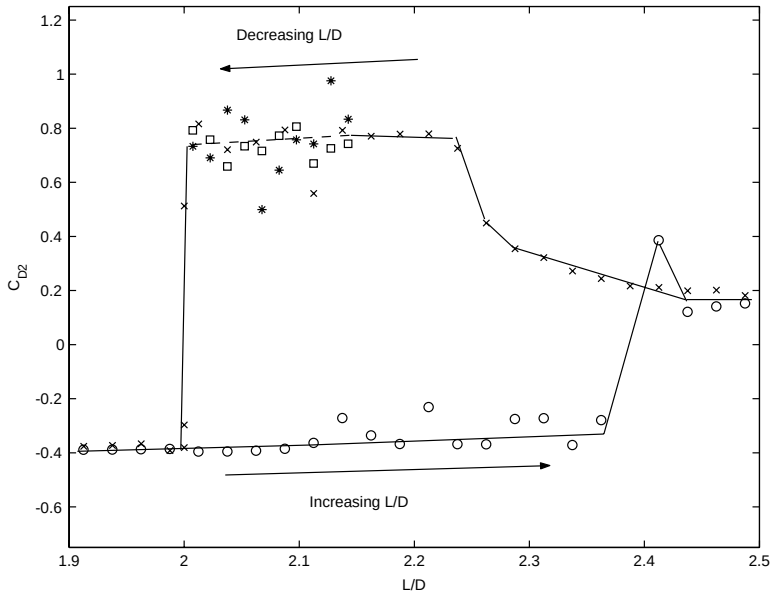

Fig. 9. Hysteresis of downstream drag coefficient, Re = 1000.

Table 1
Summary of data for Re = 1000 tandem configurations

	Upstream		downstream		
L/D	$\bar{C}_D$	$\tilde{C}_L$	$\bar{C}_D$	$\tilde{C}_L$	St
2.0	0.92	0.04	−0.39	0.12	0.17
2.15 Reattach	0.92	0.09	−0.34	0.49	0.16
2.15 T.V.S	1.35	1.44	0.78	2.22	0.17
2.5	1.43	1.35	0.17	2.25	0.22
Isolated cyl.	1.51	1.40			0.25

experimentally reported values of 3.0–3.8. As discussed above, this problem is extremely sensitive to Reynolds number, turbulence, and experimental setup, so a precise match of the transition spacing is not expected. These results are consistent with numerical results of Mittal et al. (1997) who found the *two vortex streets* regime at $L/D = 2.5$ and Re = 1000 also.

To achieve the upper branch of the hysteresis, the cylinder pair is started in the *two vortex streets* regime at $L/D = 2.5$ and the spacing is decreased to $L/D = 1.9$ in the manner described above. In this case, the *two vortex streets* regime is observed down to a spacing of $L/D \approx 2.0$ at which point a transition to the *reattachment* regime occurs. Again, consistent with experimental observations, a sharp decrease in the drag for both cylinders is observed during this transition.

In the region $2.0 < L/D < 2.2$ on the upper branch of the hysteresis, very irregular forces are observed on both the upstream and downstream cylinders. To demonstrate this, two additional simulations were performed in this region with different speeds of cylinder motion and the resulting drag coefficients are plotted on Figs. 8 and 9. In this region, the vortex shedding behind the upstream cylinder is persistent but irregular. This indicates that the *two vortex streets* regime becomes progressively more unstable as the spacing approaches the transition point at $L/D = 2.0$. A similar effect occurs near the transition from the *reattachment* regime at $2.2 < L/D < 2.4$ but the irregularity in the flow field and forces is far less significant.

Table 1 summarizes the mean drag, lift amplitude, and Strouhal number for the Re = 1000 cases presented above, along with the data for an isolated cylinder for comparison.

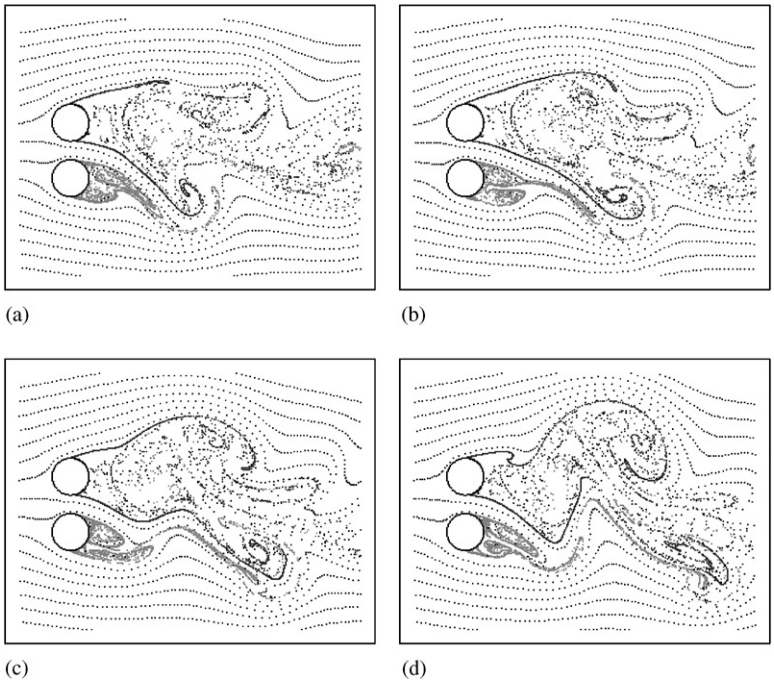

Fig. 10. Particle traces for *biased gap* Regime, Re = 1000, $T/D = 1.5$.

4.4. Side-by-side configuration

In side-by-side configurations, the two cylinders are oriented perpendicular to the incoming flow. In this configuration, there are again three primary flow regimes according to the classification of Zdravkovich (1982) and Chen (1987) as follows.

(i) *Single body* ($T/D \leqslant 1.2$). Similar to the tandem case, when the cylinders are placed side-by-side in extremely close proximity, they behave as a single body with a single vortex street.
(ii) *Biased gap* ($1.2 < T/D < 2.0$). For intermediate spacings, the flow in the gap between the cylinders is deflected towards one of the cylinders. Thus, two distinctive near wakes are formed, one wide wake and one narrow. The particular direction of the bias will intermittently change, indicating another *bistable* state.
(iii) *Coupled vortex streets* ($2.0 \leqslant T/D \leqslant 4$). In this region, two distinct vortex streets are formed. These vortex streets are usually coupled in a symmetric manner, i.e., vortices are alternatively shed on the gap-side then the outside of the cylinders.

In the present study, the *biased gap* and *coupled vortex streets* flow regimes have been simulated and analyzed at Re = 1000. Qualitative comparisons with experimental observations are excellent.

4.4.1. Biased gap regime

Particle traces for the biased gap regime ($T/D = 1.5$) are shown on Fig. 10. This figure shows four snapshots with the gap flow biased downwards. Each bias tends to persist for between five and ten periods of vortex shedding, then a transition to the other bias will tend to occur. The *flopping* between states occurs at time intervals roughly two orders of magnitude shorter than those reported in experimental results by Kim and Durbin (1988) at Re = 3500 and $T/D = 1.75$, although they are consistent with other numerical results of Chang and Song (1990). The reason for this discrepancy is not clear.

The lift and drag coefficients and Strouhal numbers for the narrow and wide wake cylinders differ noticeably. For the wide wake cylinder, the mean drag coefficient was found to be $\bar{C}_D = 1.25$ while the narrow wake cylinder had a measured mean drag of $\bar{C}_D = 1.85$. The wide wake cylinder is also associated with smaller oscillations in the lift coefficient ($\tilde{C}_L = 0.55$) and a smaller Strouhal number ($St = 0.23$) than the narrow wake cylinder ($\tilde{C}_L = 1.74, St =$

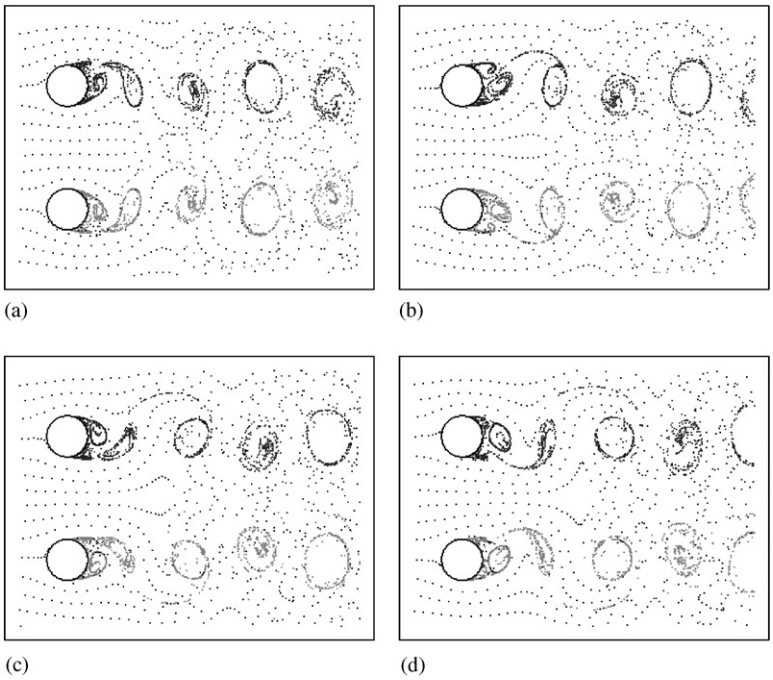

Fig. 11. Particle traces for *coupled shedding* regime, Re = 1000, $T/D = 3$.

Table 2
Summary of data for Re = 1000 side-by-side configurations

T/D	$\bar{C}_D$	$\tilde{C}_L$	St
1.5 Wide wake	1.25	0.55	0.23
1.5 Narrow wake	1.85	1.74	0.30
3.0	1.70	1.67	0.26
Isolated cyl.	1.51	1.40	0.25

0.30). These three results are all consistent with experimental observations (Bearman and Wadcock, 1973; Kiya et al., 1980; Kim and Durbin 1988) and are due to the tighter formation of vortices in the near wake of the narrow wake cylinder compared to that of the wide wake cylinder.

4.4.2. Coupled shedding regime

Four snapshots of particle traces for Re = 1000, $T/D = 3$ are shown in Fig. 11. The symmetric formation and shedding of vortices as reported by Zdravkovich (1982) and Chen (1987) is clearly observed. Other experimental results by Williamson (1985) show that an antisymmetric formation pattern is also possible, although he reports that the symmetric (or antiphase) shedding is predominant. Only this form of shedding has been observed in the numerical results.[1]

The two cylinders in this regime experienced identical drag coefficients of $\bar{C}_D = 1.70$ and Strouhal numbers of $St = 0.26$. The combined drag of the two cylinders exceeds double the value for an isolated cylinder, as determined

[1] Future simulations of moving cylinder pairs showed that the antisymmetric pattern observed experimentally can also be reproduced numerically if an in-phase oscillation is applied as an initial perturbation to the cylinders. These results will be presented in an upcoming publication.

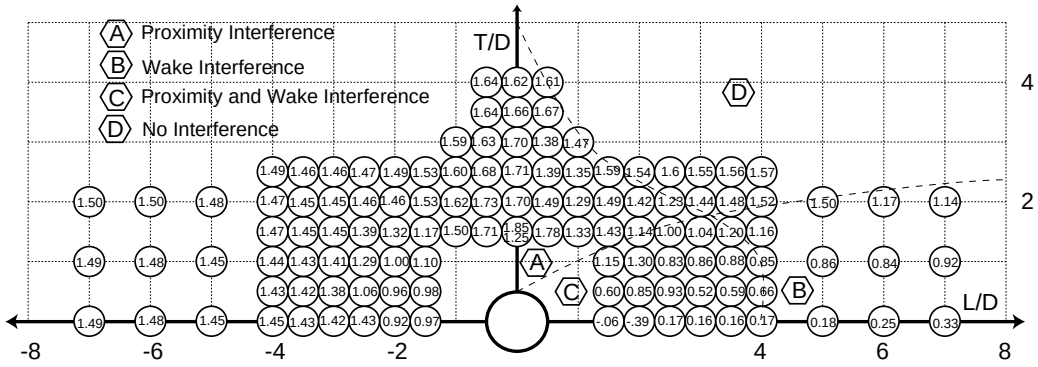

Fig. 12. Mean drag coefficients for Re = 1000 staggered arrangements with boundaries of interference regimes.

experimentally by Biermann and Herrnstein (1933). The amplitude of oscillation in the lift coefficients was also identical at $\tilde{C}_L = 1.67$, although each cylinder also experiences a nonzero mean lift coefficient which applies a repulsive force to the cylinder pair. Again, this shows excellent agreement with experimental observations from Bearman and Wadcock (1973).

Table 2 summarizes the mean drag, lift amplitude, and Strouhal number for the Re = 1000 side-by-side cases presented above, along with the data for an isolated cylinder for comparison.

4.5. Staggered configuration

The staggered configuration, where both the longitudinal and transverse spacings are nonzero, is the most common to occur in applications. Due to the limitless number of vastly different staggered configurations, relatively little comprehensive work has been performed either experimentally or numerically. The most complete experimental summary by Zdravkovich (1977, 1984) indicates three primary interference regions, as follows.

(i) *Proximity interference* is found in a side-by-side or slightly staggered arrangement with roughly four diameters of separation or less. This is usually accompanied by an increase in the mean drag coefficient for both cylinders.

(ii) *Wake interference* is found when the downstream cylinder is situated in the wake of the upstream cylinder for $L/D \geqslant 4$. The downstream cylinder experiences an irregular, retarded flow which results in a reduced mean drag coefficient. The forces on the upstream cylinder rapidly approaches that of an isolated cylinder as L/D is increased while the drag on the downstream cylinder is reduced due to the retarded flow in the wake.

(iii) *Proximity and wake interference* occurs when the downstream cylinder is in the wake of the upstream cylinder but $L/D < 4$. In this region extremely small changes in cylinder spacings can result in large changes in flow features and forces (Zdravkovich, 1977). This region includes the highly irregular bi-stable transition states described in Section 4.2.

In the present study, a series of 51 staggered cases were run with $0 \leqslant L/D \leqslant 7$ and $0 \leqslant T/D \leqslant 4$. To efficiently simulate this many different cases, a series of nine meshes and initial solutions were generated at a variety of spacings. Using the interactive steering and automatic mesh deformation/adaptation described in Section 3.6, the spacings were changed dynamically to each of the desired final values. At each spacing, the solution was run for at least 25 cycles of vortex shedding or until a converged (periodic) solution was obtained.

The measured mean drag coefficient for each of the cases is shown on Fig. 12. Data to the right of the reference cylinder at the origin represents drag values on the downstream cylinder while data to the left represents upstream cylinder values. The tandem results described in Section 4.2 are included along the horizontal axis while the side-by-side results from Section 4.4 are included along the vertical axis (including the bi-stable configuration represented by the two different drag values at $L/D = 0$, $T/D = 1.5$).

Fig. 12 also includes the rough boundaries between the different staggered interference regimes as given by Zdravkovich (1977). Following Fig. 12, several observations consistent with experimental data are made.

5. Conclusions

This paper has presented the results of an extensive numerical investigation into interference effects between cylinder pairs. The numerical method, based on a second order SUPG projection scheme, coupled with interactive simulation tools and dynamic meshes, has allowed for an unprecedented study of the problem.

Direct quantitative comparison with available low Reynolds number results have been encouraging. Furthermore, the first extensive numerical observation of flow physics such as bi-stable flowstates and hysteresis effects in flow about cylinder pairs has been demonstrated. An extensive series of 51 simulations in various staggered arrangements was also performed, which demonstrated the correct prediction of both wake-interference and proximity-interference effects. Although the exact spacings and force coefficients associated with these flow regimes cannot be matched exactly with experimental results which include turbulent and 3-D effects, the correlation of flow regimes and trends in force coefficients show good agreement.

These results lead to the conclusion that numerical simulation of unsteady incompressible flows is capable of reproducing in great detail the complex unsteady interactions between bluff bodies. Furthermore, the interactive simulation techniques developed in this work allow the rapid simulation of a large number of configurations and a detailed study of transitional states between known interference regimes.

The natural extension of this work is to consider the effects of interference on structural response and vortex-induced vibrations. This work is well underway, using the existing methods for mesh movement to accommodate arbitrary flow-induced motion of both bodies. Ultimately, this effort should lead to a deeper understanding of interference effects in actual engineering applications.

Acknowledgements

This work was supported in part by a Joint Industry Project in cooperation with BP-Amoco, Chevron, Deep Oil Technology, Exxon-Mobil, Global Marine, MARIN Netherlands, Shell, Statoil, and UNOCAL. Additional funding was obtained from the Offshore Technology Research Center (OTRC) and the Texas Advanced Technology Program (ATP) # 0442-1999.

References

Batina, J.T., 1991. Unsteady Euler algorithm with unstructured dynamic mesh for complex aircraft aerodynamic analysis. AIAA Journal 29, 327–333.

Bearman, P.W., Wadcock, A.J., 1973. The interaction between a pair of circular cylinders normal to a stream. Journal of Fluid Mechanics 61, 499–511.

Behr, M., Johnson, A., Kennedy, J., Mittal, S., Tezduyar, T.E., 1993. Computation of incompressible flows with inplicit finite element implementations on the connection machine. Computational Methods in Applied Mechanics and Engineering 108, 99–118.

Bercovier, M., Pironneau, O., 1979. Error estimates for finite element method solution of the Stokes problem in the primitive variables. Numerische Mathematik 33, 211–224.

Biermann, D., Herrnstein, W.H., 1933. The interference between struts in various combinations, Technical Report 468, National Advisory Committee for Aeronautics.

Blevins, R., 1990. Flow-Induced Vibration. Van Nostrand Reinhold, New York.

Brooks, A., Hughes, T., 1982. Streamline Upwind/Petrov–Galerkin formulations for convection dominated flows with particular emphasis on the incompressible Navier–Stokes equations. Computational Methods in Applied Mechanics and Engineering 32, 199–259.

Cahouet, J., Chabard, J., 1988. Some fast 3D finite element solvers for the generalized Stokes problem. International Journal for Numerical Methods in Fluids 8, 869–895.

Chang, K., Song, C., 1990. Interactive vortex shedding from a pair of circular cylinders in a transverse arrangement. International Journal for Numerical Methods in Fluids 11, 317–329.

Chen, S.-S., 1987. Flow-Induced Vibration of Circular Cylindrical Structures. Hemisphere Publishing Company, Washington.

Chen, A., Kallinderis, Y., 1998. Adaptive hybrid (prismatic/tetrahedral) grids for incompressible flows. International Journal for Numerical Methods in Fluids 26, 1085–1105.

Codina, R., Oñate, E., Cervera, M., 1992. The intrinsic time for the streamline upwind/Petrov–Galerkin formulation using quadratic elements. Computational Methods in Applied Mechanics and Engineering 94, 239–262.

Edis, F., Aslan, R., 1998. Efficient incompressible flow calculations using pQ2Q1 element. Communications in Numerical Methods in Engineering 14, 161–178.

Farhat, C., Degand, C., Koobus, B., Lesoinne, M., 1998. Torsional springs for two-dimensional dynamic unstructured fluid meshes. Computational Methods in Applied Mechanics and Engineering 163, 231–245.

Golub, G., van Loan, C., 1996. Matrix Computations. The Johns Hopkins University Press, Baltimore, MD.

Gresho, P., 1990. On the theory of semi-implicit projection methods for viscous incompressible flow and its implementation via a finite element method that also introduces a consistent mass matrix, Part 1: theory. International Journal for Numerical Methods in Fluids 11, 587–620.

Gresho, P., Chan, S., 1990. On the theory of semi-implicit projection methods for viscous incompressible flow and its implementation via a finite element method that also introduces a consistent mass matrix, Part 2: implementation. International Journal for Numerical Methods in Fluids 11, 621–660.

Guermond, J., Quartapelle, L., 1998. On incremental projection methods. In: Salvi, R. (Ed.), Navier–Stokes Equations: Theory and Numerical Methods. Longman, Harlow, pp. 277–288.

Gunzburger, M., 1989. Finite Element Methods for Viscous Incompressible Flows. Academic Press, Boston.

Hassan, O., Probert, E.J., Morgan, K., 1998. Unstructured mesh procedures for the simulation of three-dimensional transient compressible inviscid flows with moving boundary components. International Journal for Numerical Methods in Fluids 27, 41–55.

Hughes, T., Liu, W., Zimmerman, T., 1981. Lagrangian–Eulerian finite element formulation for incompressible viscous flows. Computational Methods in Applied Mechanics and Engineering 29, 329–349.

Ishigai, S., Nishikawa, E., Nishimura, K., Cho, K., 1972. Experimental study on structure of gas flow in tube banks with tube axes normal to flow. Bulletin of JSME 15, 949–956.

Kallinderis, Y., Nakajima, K., 1994. Finite element method for incompressible viscous flows with adaptive hybrid grids. AIAA Journal 32, 1617–1625.

Kim, H.J., Durbin, P.A., 1988. Investigation of the flow between a pair of circular cylinders in the flopping regime. Journal of Fluid Mechanics 196, 431–448.

King, R., Johns, D., 1976. Wake interaction experiments with two flexible circular cylinders in flowing water. Journal of Sound and Vibration 45, 259–283.

Kiya, M., Arie, M., Tamura, H., Mori, H., 1980. Vortex shedding from two circular cylinders in staggered arrangements. ASME Journal of Fluids Engineering 102, 166–173.

Kiya, M., Mochizuki, O., Ido, Y., Suzuki, T., Arai, T., 1992. Flip-flopping flow around two bluff bodies in tandem arrangement. In: Eckelmann, H., Graham, J.M.R., Huerre, P., Monkewitz, P.A. (Eds.), Bluff-Body Wakes, Dynamics and Instabilities. Springer, Berlin, pp. 15–18.

Kostic, Z.G., Oka, S.N., 1972. Fluid flow and heat transfer with two cylinders in cross flow. International Journal of Heat and Mass Transfer 15, 279–299.

Lei, C., Cheng, L., Kavanagh, K., 2000. A finite difference solution of the shear flow over a circular cylinder. Ocean Engineering 27, 271–290.

Mittal, S., Kumar, V., Raghuvanshi, A., 1997. Unsteady incompressible flows past two cylinders in tandem and staggered arrangements. International Journal for Numerical Methods in Fluids 25, 1315–1344.

Nagai, S., Kurata, K., 1971. Interference between cylinders in an open channel flow. Transactions of the Japanese Society of Civil Engineering 3, 200–201.

Nomura, T., Hughes, T., 1992. An arbitrary Lagrangian–Eulerian finite element method for interaction of fluid and a rigid body. Computational Methods in Applied Mechanics and Engineering 95, 115–138.

Norburn, S., Silvester, D., 1998. Stabilised vs. stable mixed methods for incompressible flow. Computational Methods in Applied Mechanics and Engineering 166, 131–141.

Pannell, J.R., Griffiths, E.A., Coales, J.D., 1915. Experiments on the interference between pairs of aeroplane wires of circular and lenticular cross section. Advisory Committee for Aeronautics. Reports and Memoranda 7, 219–221.

Schulz, K., Kallinderis, Y., 1998a. Numerical flow structure interaction for cylinders undergoing vortex-induced vibrations. Technical Report OTC 8699, Offshore Technology Conference.

Schulz, K., Kallinderis, Y., 1998b. Unsteady flow structure interaction for incompressible flows using deformable hybrid grids. Journal of Computational Physics 143, 569–597.

Schulz, K., Kallinderis, Y., 2000. Three-dimensional numerical prediction of the hydrodynamic loads and motions of offshore structures. Proceedings of ETCE/OMAE2000 Joint Conference, Energy for the New Millennium, No. 00-4190 in OTC.

Sumner, D., Price, S.J., Païdoussis, M.P., 2000. Flow-pattern identification for two staggered circular cylinders in cross-flow. Journal of Fluid Mechanics 411, 263–303.

Tanida, Y., Okajima, A., Watanabe, Y., 1973. Stability of a circular cylinder oscillating in uniform flow or in a wake. Journal of Fluid Mechanics 41, 769–784.

Thomas, D., Kraus, K., 1964. Interaction of vortex streets. Journal of Applied Physics 35, 3458–3459.

Trépanier, J.Y., Reggio, M., Paraschivoiu, M., Camarero, R., 1993. Unsteady Euler solutions for arbitrarily moving bodies and boundaries. AIAA Journal 31, 1869–1876.

Verfurth, R., 1984. Error estimates for a mixed finite element approximation of the Stokes equations. RAIRO: Numerical Analysis 18, 175–182.

Williamson, C.H.K., 1985. Evolution of a single wake behind a pair of bluff bodies. Journal of Fluid Mechanics 159, 1–18.

Zdravkovich, M.M., 1977. Review of flow interference between two circular cylinders in various arrangements. ASME Journal of Fluids Engineering 99, 618–633.

Zdravkovich, M.M. 1982. Flow induced oscillations of two interfering circular cylinders. International Conference on Flow Induced Vibrations in Fluid Engineering, Reading, No. D2.

Zdravkovich, M.M., 1984. Classification of flow-induced oscillations of two parallel circular cylinders in various arrangements. Symposium on Flow-Induced Vibrations, Vol. 2, pp. 1–18.

Zdravkovich, M.M., 1985. Flow induced oscillations of two interfering circular cylinders. Journal of Sound and Vibration 101, 511–521.

Zdravkovich, M.M., 1997. Flow Around Circular Cylinders Vol 1: Fundamentals. Oxford University Press, Oxford.